Controlling nanomagnet magnetization dynamics via magnetoelastic coupling

Y. Yahagi, B. Harteneck, S. Cabrini, and H. Schmidt

Phys. Rev. B **90**, 140405 — Published 30 October 2014

DOI: 10.1103/PhysRevB.90.140405

Controlling nanomagnet magnetization dynamics via magneto-elastic coupling

Y. Yahagi[1], B. Harteneck[2], S. Cabrini[2], and H. Schmidt[1*]

[1] *School of Engineering, University of California Santa Cruz, 1156 High Street, Santa Cruz, California 95064, USA*

[2] *Molecular Foundry, Lawrence Berkeley National Laboratory, California 94720, USA.*

[*] *Corresponding author: hschmidt@soe.ucsc.edu*

We demonstrate that elastic interactions between nanomagnets in a periodic array can determine the magnetic response according to the nanoscale array geometry. These findings are attributed to magneto-elastic coupling of the spin dynamics with simultaneously excited surface acoustic waves. Specifically, we observe three manifestations of this effect: pinning of the magnetic resonance frequency over an extended range of applied magnetic fields, generation of additional modes whose frequency can differ by more than 100% from the intrinsic element response, and an enhancement of the Fourier amplitude of the magnetic mode at crossovers with mechanical modes. Simulations of the dynamics in the presence of coupling between magnetic and mechanical degrees of freedom are in good agreement with the experiment. This suggests that magnetization dynamics can be controlled by rational structural design on the nanoscale even when the magnetostatic interactions are negligible.

PACS numbers: 75.75Jn, 75.78.Jp,

Dynamic processes in nanomagnets have received increasing attention both due to their potential applications in next-generation spintronic devices for data recording and because of fundamental understanding of magnetism that can be gained from small single-domain magnetic structures. A variety of techniques including ferromagnetic resonance [1], Brillouin light scattering [2], X-ray spectroscopy [3], and the time-resolved magneto-optic Kerr effect (TR-MOKE) [4-8] have been used to access dynamic processes on the pico- and femtosecond time scale. Studies on single nanomagnets as well as ensemble measurements have revealed the influence of the two- and three-dimensional shape [4,5] and the fabrication process [2] of the individual nanomagnets on the spin wave spectrum. It has also been shown that *magnetic* interactions between densely packed magnets result in deviations from single magnet behavior in terms of resonance frequency shifts [8] and dynamic dephasing (damping) of the ensemble signal [9]. Periodic arrays of *non-magnetic* materials, on the other hand, were shown to exhibit oscillations in their time-dependent reflectivity due to the generation of elastic waves in these phononic crystals [10,11]. Several groups have recently observed that acoustic waves can trigger magnetization precessions and even switching in *continuous magnetic films* via magneto-elastic coupling [12-18]. However, the interplay between phononic and magnetic modes generated in nanostructured array and its effect on the magnetization dynamics of a nanomagnet has not been investigated. This question has both fundamental and technological importance since densely packed nanomagnet arrays will form the basis of bit-patterned media, MRAM, and other spintronic devices.

Here, we demonstrate the optical generation and detection of both mechanical and magnetic modes in the same nanomagnet array. We show that mechanical surface acoustic waves (SAWs) strongly influence the magnetization dynamics of the nanomagnets via magneto-elastic coupling. The interplay between these fundamental excitations manifests itself in multiple ways: First, we observe pinning of the magnetic resonance frequencies at several points over an extended range of applied field. Secondly, new magnetic oscillation modes are generated at frequencies entirely determined by the lattice structure of the array and neither shape nor material of the nanomagnets. Finally, the Fourier amplitude of the magnetization precession mode is strongly enhanced at applied magnetic fields where the SAW and intrinsic magnetic frequency are degenerate. This behavior is reproduced with a model that takes into account both mechanical and magnetic oscillations. This demonstrates that the magnetic response of a nanomagnet array is heavily influenced by its physical geometry and the mechanical properties of the substrate.

The study was carried out on arrays of 30-nm thick nickel elliptic disks with varying array pitch *p* (Fig. 1a) fabricated using electron beam lithography with electron beam deposition and liftoff on a (100) silicon substrate with a 110-nm thick hafnium oxide antireflection (AR) coating that helps maximize the magneto-optical signal [8,19]. The major and minor diameters of the ellipses were 140 and 80 nm, respectively, as measured by scanning electron microscopy. Control samples with equally patterned aluminum disks and an unpatterned nickel film were also prepared. The dynamic response of the nanostructures was measured with a previously described two-color TR-MOKE setup [5]. Briefly, 165-fs long pulses from a Coherent Mira Ti:sapphire laser were split into pump (wavelength 400 nm; $1/e^2$ spot diameter 10 μm) and probe (800 nm; 6 μm) pulses and focused on the sample using a 60× microscope objective (N.A. = 0.85). The probe beam traveled through a linear polarizer and an optical delay line to provide sub-picosecond temporal resolution (Fig. 1b). The changes in both polarization and total reflected power of the probe beam were measured using a balanced photodetector configuration, yielding both the magnetic (difference signal) and non-magnetic (sum signal) response of the sample. In addition to initiating a magnetization precession in the nanomagnets [20], the optical pump pulse heats up the nanomagnets and causes impulsive expansion. This induces spatially modulated stress in the substrate and launches SAWs propagating along its surface as will be shown below. A variable external magnetic field with an in-plane component oriented along the major axis of the ellipses and an inclination of 60^o relative to the sample surface was applied using permanent magnets (Fig. 1b).

Fig. 2 shows the background-corrected [5] time-resolved optical response of the three sample types divided into magnetic (difference signal) and non-magnetic (sum signal) channels along with the corresponding Fourier-transformed power spectra. The vertical scale of the detected signal is the same for each pair. The nickel film (Fig. 2a) exhibits a clean single-frequency oscillation at an applied field of 2 kOe due to magnetic precession of the Kittel mode [21]. The absence of any non-magnetic signal illustrates the clean separation of channels in the balanced photodetector setup. The colormap in Fig. 2d shows the magnetic film response versus applied magnetic field. A single resonance peak appears at each field value in excellent agreement with the analytic solution of the Kittel mode (dashed line), assuming a Lande factor $g = 2.21$ and a saturation magnetization $M_s = 341$ emu/cm^3. Using M_s as a fitting parameter also accounts for uncertainties in the magnet size, shape, and the magnetic field value at the nanomagnet location. These parameters were used in the subsequent micromagnetic simulations. The patterned Al disks, on the other hand (Fig. 2b) exhibit a multi-mode spectrum in the non-magnetic channel. Only a very small signal in the magnetic channel due to imperfect balancing of the photodiodes is observed. The non-magnetic oscillations in sample reflectivity can be attributed to surface acoustic waves (SAWs) generated by the pump pulse heating the metallic elements in the nanostructured sample analogous to non-magnetic nanostructures [10]. For small mass loading, these SAW frequencies can be calculated by the ratio of the phase velocity v and the wavelength λ of the acoustic wave in the substrate. Here, λ is determined by the periodicity D of the array along various directions [10,11]. The four dark arrows in Fig. 2b (right) denote the lowest Rayleigh wave (RW) frequencies (corresponding to $D = p$, $p/\sqrt{2}$, $p/2$, and $p/\sqrt{5}$) predicted for $v = 2400$ m/s in good agreement with the experiment. Note that the RW frequencies are predominantly determined by the elastic properties of the AR coating layer, where the majority of the elastic energy is confined. Due to the elliptic shape of the nanoelements, SAW modes along x and y-directions are non-degenerate. However, the splitting is much smaller than the width of the Fourier peaks which is confirmed by simulations (see below). In addition to the RW frequencies, an additional feature at 17.6 GHz is observed (gray arrow). This peak is attributed to the surface skimming longitudinal wave (SSLW) [22] and will be discussed below.

Fig. 2c shows the dynamic response of the patterned nickel disks at an applied field of 2 kOe. Now we observe oscillations in both magnetic and non-magnetic channels. The magnetic signal can be attributed to the interplay between the Kittel mode shifted from the film mode due to the internal demagnetization field [4] and elastic waves. The SAW frequencies in the non-magnetic channel (indicated with arrows in Fig. 2c) agree with those of the non-magnetic nanostructures, validating the assumption of negligible mass loading [11,23,24]. This shows that we excited a magnetic response determined by the material and dimensions of the individual nanomagnets and a non-magnetic, mechanical response determined by the substrate material and the geometric design of the nanopatterned array. This is the principal result of this paper.

In order to investigate the interplay between these physically distinct phenomena, we carried out a series of measurements at different applied fields. The results are displayed in Fig. 3. As expected, the non-magnetic frequencies are field-independent (Fig. 3a). The magnetic channel, on the other hand, shows an unexpected and complex response. Fig. 3b shows a normalized colormap analogous to the unpatterned film in Fig. 2d, in which the highest Fourier peak at each field strength is assigned a value of 1. In sharp contrast to the single, continuous band of Fig. 2d, we find a fragmented, multi-mode response at fields >2.5 kOe. At low fields, we observe a single Kittel mode, qualitatively similar to the film response (Fig. 2d), but modified by the shape-dependent demagnetization field and magneto-static interelement interactions. The latter are much smaller than previously reported configurations [8] due to the smaller stray field from the thinner and smaller nanomagnets. The low-field behavior is in excellent agreement with simulations that include only these magnetic contributions (dashed line). However, at higher fields we notice an extended band at ~12.2 GHz where the magnetic response is "pinned" over a range of more than 2 kOe. A similar pinning effect is observed at 15.8, 17.7, and 22.3 GHz. Moreover, we find the generation of additional magnetic oscillations at frequencies far removed (up to 120% larger than the Kittel mode at 3 kOe) from the response expected from a single element.

If we plot the absolute Fourier amplitudes directly obtained from the TR-MOKE signal in the "non-normalized" display (Fig. 3d), we can still identify traces of the Kittel mode (simulations shown with dashed line). However, regions with the highest Fourier amplitudes are seen at 12.2, 15.8, 17.7, and 22.3 GHz. These coincide with the non-magnetic SAW frequencies and suggest strong coupling between mechanical and magnetic degrees of freedom at the crossover points.

In order to elucidate this coupling mechanism, we implemented a multi-step modeling process. First, we obtained the time evolution of the lattice temperature with a three-temperature model [25] in a nickel elliptic disk with the parameters specified in [26]. At the measured pump fluence of 0.78 mJ/cm^2, the lattice temperature in the simulation rises by 25 K in 8 ps. The subsequent thermal expansion and elastic motion were simulated with finite element analysis of the dynamic equation of motion

$$\rho \frac{\partial^2 u_i}{\partial t^2} = \sum_{j=1}^{3} \frac{\partial \sigma_{ji}}{\partial x_j}, \qquad (1)$$

where i, j = 1, 2, 3 denote the Cartesian coordinates, ρ is the density, u_i is the displacement, and σ_{ij} is the Cauchy stress tensor. The simulated displacement is converted to elastic strain $\varepsilon_{ij}(\vec{r},t) = \left(\partial u_i/\partial x_j + \partial u_j/\partial x_i\right)/2$. A unit cell of the simulations consists of a nickel elliptic disk on the AR coating layer and substrate with periodic boundary conditions on the sidewalls. The simulation parameters are specified in [26]. The Young's modulus E = 161 GPa of the AR coating layer is determined by matching the three lowest RW frequencies to the measurements with a least square method. Using the initial magnetization of the nanomagnet calculated with Object-Oriented Micromagnetic Framework (OOMMF) [27] and the simulated strain field, we obtain the magneto-elastic energy density

$$U_{\mathrm{mel}} = \frac{B_1}{M_{\mathrm{S}}^2} \sum_i M_i^2 \varepsilon_{ii} + \frac{B_2}{M_{\mathrm{S}}^2} \sum_i \sum_{j \neq i} M_i M_j \varepsilon_{ij} , \qquad (2)$$

where M_{S} is the saturation magnetization, $M_{\mathrm{i,j}}$ are the magnetization component along axes i, j, and B_1, B_2 are the magneto-elastic constants [28]. We verified that additional terms due to exchange coupling can be neglected [26]. An additional magnetic field contribution due to magneto-elastic coupling is then calculated via the variational derivative

$$H_{\mathrm{mel}} = -\frac{\delta U_{\mathrm{mel}}}{\delta \vec{M}} = -\frac{\partial U_{\mathrm{mel}}}{\partial \vec{M}} + \sum_i \frac{\partial}{\partial x_i} \left[\frac{\partial U_{\mathrm{mel}}}{\partial \left(\frac{\partial \vec{M}}{\partial x_i} \right)} \right] \qquad (3)$$

and added to the effective field for the dynamic simulations of the magnetization dynamics with OOMMF. The simplifying assumption of neglecting the back-action of the magnetization dynamics on the elasticity has successfully been used previously to analyze magneto-elastic dynamics in nickel films [15]. Here, it is also justified by the fact that the non-magnetic signal shows no observable change at the crossover points. With $B_1 = B_2 = 7.85\times10^7$ erg/cm^3 for polycrystalline nickel [15], the calculated H_{mel} has an oscillation amplitude of 170 Oe at 100 ps after the optical excitation at the center of the elliptic nanomagnet along its major axis. The simulated magnetization dynamics in the presence of magneto-elastic coupling were Fourier transformed and displayed in Figs. 3c and 3e. We find that the simulations are in excellent qualitative agreement with the experiment and confirm that magneto-elastic coupling is at the heart of the complex magnetic response of the patterned disk arrays. Specifically, the simulations correctly predict the mode pinning at 12.4, 16.0, 17.9, and 21.1 GHz over the wide applied field range. Moreover, the simulated non-normalized response correctly reproduces the enhanced Fourier amplitudes at the crossover frequencies of the intrinsic magnetic modes with the elastic modes (Figs. 3d,e). These are the result of prolonged precession at these frequencies, which is also evident from the time traces. Finally, we note that the simulations also correctly predict the mode at 17.9 GHz (dashed arrow in Fig. 3b), which corresponds to a surface skimming longitudinal wave (SSLW) with predominantly in-plane displacement and higher phase velocity than a Rayleigh wave [22]. This assignment was confirmed with space-time discrete Fourier transform analysis of the simulated displacement.

These results suggest the possibility of tuning the magnetic response of physically identical nanomagnets by changing the geometric arrangement of the array. In order to demonstrate this design freedom, we investigated an array of identical nickel disks, but with larger pitch ($p = 282$ nm). Experiments and simulations were carried out in the same way as for the more densely packed array and are shown in Fig. 4. We find a shift of the non-magnetic SAW peaks to lower frequencies due to the larger pitch as predicted by v/D. Consequently, hot spots of increased Fourier amplitudes and pinned magnetic resonances appear at different crossing points (applied fields) determined by the SAW frequencies in both experiment and simulations. The RWs and SSLW are identified as solid and dashed arrows in Fig. 4b and are again predicted accurately by the model. In contrast to the strong dependence on pitch, we found no dependence of the magnetic spin wave spectra on optical pump power over a wide range in either experiment or simulation. This observation is consistent with a linear dependence of the induced strain on pump power.

We have investigated the dynamic response of densely patterned nickel nanomagnet arrays and found that both mechanical and magnetic modes can be excited simultaneously by an optical pump pulse. Strong coupling between these phenomena is observed when they are brought near degeneracy by an applied magnetic field. In particular, increased Fourier amplitudes at the degeneracy points and a pinning of the magnetic resonance at elastic modes were observed over a wide field range. Both features are attributed to an additional effective field component generated by magneto-elastic coupling and were accurately reproduced by simulations. In addition, these mechanical modes trigger magnetic oscillations at frequencies far removed from the intrinsic response of the individual nanomagnet. The SAW frequencies are to first order unrelated to the shape, size, and material of the nanomagnetic elements and can be tuned independently via the array geometry and the choice of substrate material. This opens interesting perspectives for the design of nanomagnetic and spintronic devices based on densely packed nanomagnets. Even if magnetostatic coupling between elements can be neglected (as is the case here), the array geometry can play a crucial role in determining magnetic responses. If unwanted, this coupling could be eliminated by an aperiodic design of the nanomagnet pattern. Alternatively, the pattern design can be an important control parameter. One could generate differing magnetic responses from identical elements by varying the array pitch across a sample. One could also take advantage of the increased magnetic response at the crossing point to amplify the magneto-optic response from small nanomagnets to generate elastically triggered switching [17,18,29] or assist with optically induced magnetization switching [30]. Finally, the coupling strength and crossover frequencies can be controlled experimentally by other parameters such as the orientation of the applied field which shifts the Kittel-like magnetic response without affecting the SAWs.

This work was supported by the National Science Foundation under Grant No. DMR-1311744. Work at the Molecular Foundry, Lawrence Berkeley National Laboratory was supported by the Office of Science, Office of Basic Energy Sciences, of the U.S. Department of Energy under Contract No. DE-AC02-05CH11231. We acknowledge T. Yuzvinsky and the W.M. Keck Center for Nanoscale Optofluidics at the University of California at Santa Cruz for SEM imaging.

References

[1] K. S. Buchanan, M. Grimsditch, F. Y. Fradin, S. D. Bader, and V. Novosad, Phys. Rev. Lett. **99**, 267201 (2007).

[2] H. T. Nembach, J. M. Shaw, T. J. Silva, W. L. Johnson, S. A. Kim, R. D. McMichael, and P. Kabos, Phys. Rev. B **83**, 094427 (2011).

[3] C. La-O-Vorakiat, M. Siemens, M. M. Murnane, H. C. Kapteyn, S. Mathias, M. Aeschlimann, P. Grychtol, R. Adam, C. M. Schneider, J. M. Shaw, H. Nembach, and T. J. Silva, Phys. Rev. Lett. **103**, 257402 (2009).

[4] A. Barman, S. Wang, J. D. Maas, A. R. Hawkins, S. Kwon, A. Liddle, J. Bokor, and H. Schmidt, Nano Lett. **6**, 2939 (2006).

[5] R. Brandt, F. Ganss, R. Rückriem, T. Senn, C. Brombacher, P. Krone, M. Albrecht, and H. Schmidt, Phys. Rev. B **86**, 094426 (2012).

[6] J. Hohlfeld, T. Gerrits, M. Bilderbeek, T. Rasing, H. Awano, and N. Ohta, Phys. Rev. B **65**, 012413 (2001).

[7] V. V. Kruglyak, A. Barman, R. J. Hicken, J. R. Childress, and J. A. Katine, Phys. Rev. B **71**, 220409 (2005).

[8] Z. Liu, R. Brandt, Y. Yahagi, B. Hansen, B. Harteneck, J. Bokor, A. R. Hawkins, and H. Schmidt, Appl. Phys. Lett. **98**, 052502 (2011).

[9] A. Barman and S. Barman, Phys. Rev. B **79**, 144415 (2009).

[10] J.-F. Robillard, A. Devos, and I. Roch-Jeune, Phys. Rev. B **76**, 092301 (2007).

[11] C. Giannetti, B. Revaz, F. Banfi, M. Montagnese, G. Ferrini, F. Cilento, S. Maccalli, P. Vavassori, G. Oliviero, E. Bontempi, L. E. Depero, V. Metlushko, and F. Parmigiani, Phys. Rev. B **76**, 125413 (2007).

[12] A. V. Scherbakov, A. S. Salasyuk, A. V. Akimov, X. Liu, M. Bombeck, C. Brüggemann, D. R. Yakovlev, V. F. Sapega, J. K. Furdyna, and M. Bayer, Phys. Rev. Lett. **105**, 117204 (2010).

[13] M. Bombeck, A. S. Salasyuk, B. A. Glavin, A. V. Scherbakov, C. Brüggemann, D. R. Yakovlev, V. F. Sapega, X. Liu, J. K. Furdyna, A. V. Akimov, and M. Bayer, Phys. Rev. B **85**, 195324 (2012).

[14] M. Bombeck, J. V. Jäger, A. V. Scherbakov, T. Linnik, D. R. Yakovlev, X. Liu, J. K. Furdyna, A. V. Akimov, and M. Bayer, Phys. Rev. B **87**, 060302(R) (2013).

[15] L. Dreher, M. Weiler, M. Pernpeintner, H. Huebl, R. Gross, M. S. Brandt, and S. T. B. Goennenwein, Phys. Rev. B **86**, 134415 (2012).

[16] J.-W. Kim, M. Vomir, and J.-Y. Bigot, Phys. Rev. Lett. **109**, 166601 (2012).

[17] A. Casiraghi, P. Walker, A. V. Akimov, K. W. Edmonds, A. W. Rushforth, E. De Ranieri, R. P. Campion, B. L. Gallagher, and A. J. Kent, Appl. Phys. Lett. **99**, 262503 (2011).

[18] L. Thevenard, J.-Y. Duquesne, E. Peronne, H. von Bardeleben, H. Jaffres, S. Ruttala, J.-M. George, A. Lemaître, and C. Gourdon, Phys. Rev. B **87**, 144402 (2013).

[19] S. Wang, A. Barman, H. Schmidt, J. D. Maas, A. R. Hawkins, S. Kwon, B. Harteneck, S. Cabrini, and J. Bokor, Appl. Phys. Lett. **90**, 252504 (2007).

[20] E. Beaurepaire, J.-C. Merle, A. Daunois, and J.-Y. Bigot, Phys. Rev. Lett. **76**, 4250 (1996).

[21] C. Chappert, K. Le Dang, P. Beauvillain, H. Hurdequint, and D. Renard, Phys. Rev. B **34**, 3192 (1986).

[22] T. Saito, O. Matsuda, M. Tomoda, and O. B. Wright, J. Opt. Soc. Am. B, **27**, 2632 (2010).

[23] J. Sadhu, J. H. Lee, and S. Sinha, Appl. Phys. Lett. **97**, 133106 (2010).

[24] D. Nardi, F. Banfi, C. Giannetti, B. Revaz, G. Ferrini, and F. Parmigiani, Phys. Rev. B **80**, 104119 (2009).

[25] T. Saito, O. Matsuda, and O. Wright, Phys. Rev. B **67**, 205421 (2003).

[26] See Supplemental Material at [URL] for additional simulation parameters and a discussion of additional exchange terms in magneto-elastic energy density in Eq. (2).

[27] M. Donahue and D. G. Porter, OOMMF User's guide, Version 1.0, Interagency Report NISTIR 6376, National Institute of Standard and Technology, Gaithersburg, MD (1999): URL: http://math.nist.gov/oommf.; parameters used: mesh size smaller than 5nm x 5nm x 5nm; Gilbert damping constant: α=0.05.

[28] A. G. Gurevich and G. A. Melkov, Magnetization Oscillations and Waves, (CRC Press, New York, 1996).

[29] O. Kovalenko, T. Pezeril, and V. V. Temnov, Phys. Rev. Lett., **110**, 266602 (2013).

[30] C.D. Stanciu, F. Hansteen, A.V. Kimel, A. Kirilyuk, A. Tsukamoto, A. Itoh, and T. Rasing, Phys. Rev. Lett. **99**, 047601 (2007).

FIGURES

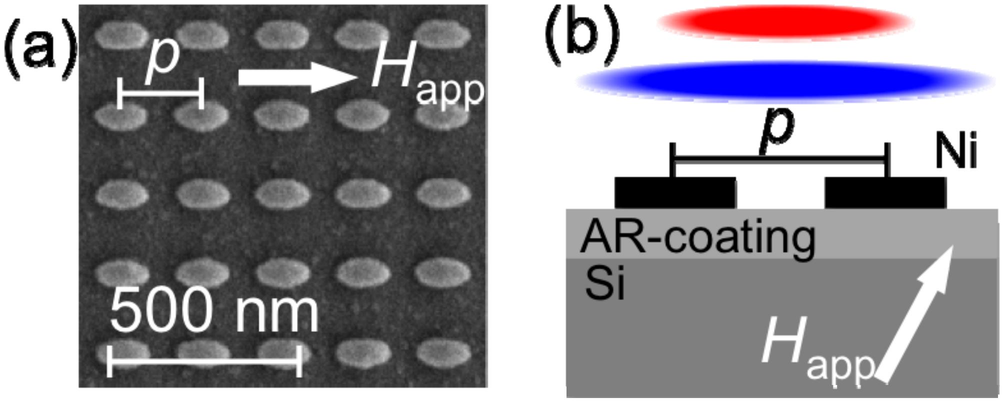

Figure 1: (a) SEM image of nickel nanomagnet arrays indicating array pitch *p* and orientation of in-plane component of applied magnetic field; (b) schematic side view of nanomagnet array showing substrate structure and two-color pump-probe arrangement with the differently sized pump and probe pulses.

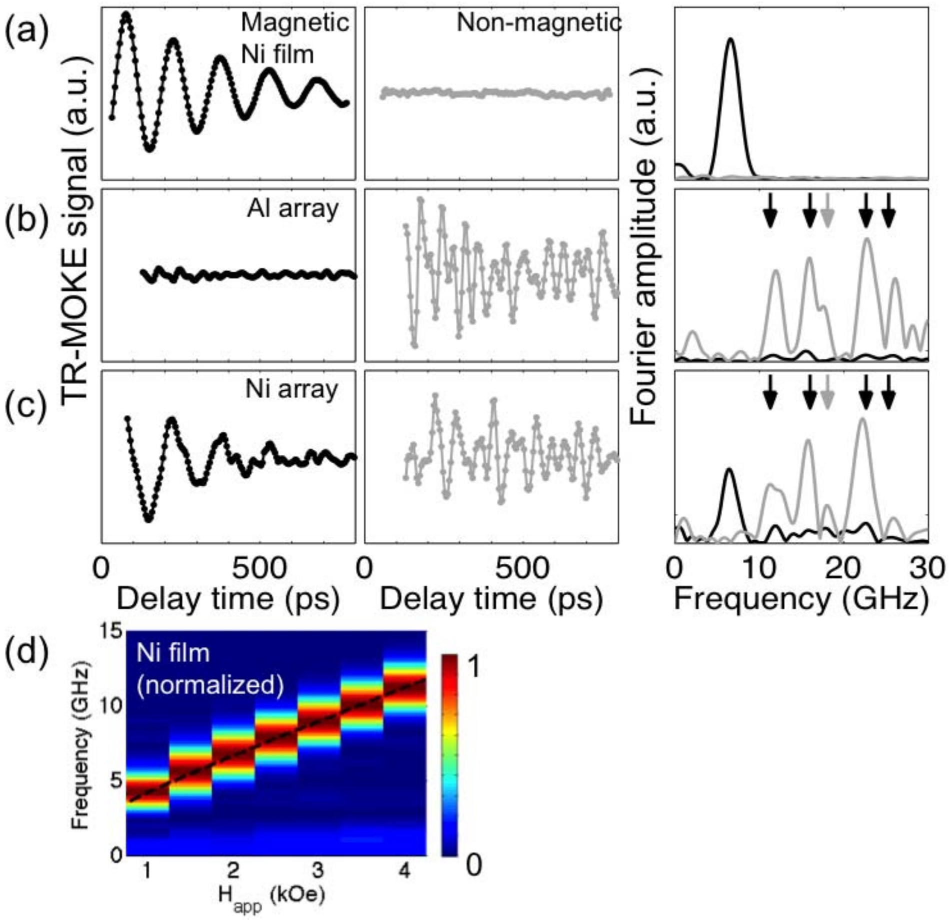

Figure 2 (Color online): (a-c) Background-subtracted TR-MOKE signal measured on (a) a nickel film, (b) an array of aluminum elliptic disks, and (c) an array of nickel elliptic disks for H_{app} = 2 kOe. The left and the center columns show the oscillations of the magnetic and non-magnetic channels, respectively, plotted on the same scale for each sample. The right column shows the Fourier spectra of the magnetic (black) and non-magnetic (light gray) signals. In (b) and (c), the dark and gray arrows show the predicted RW and SSLW frequencies, respectively. (d) Normalized Fourier spectra measured on the nickel film at different applied fields. The dashed line represents the fit with the Kittel equation.

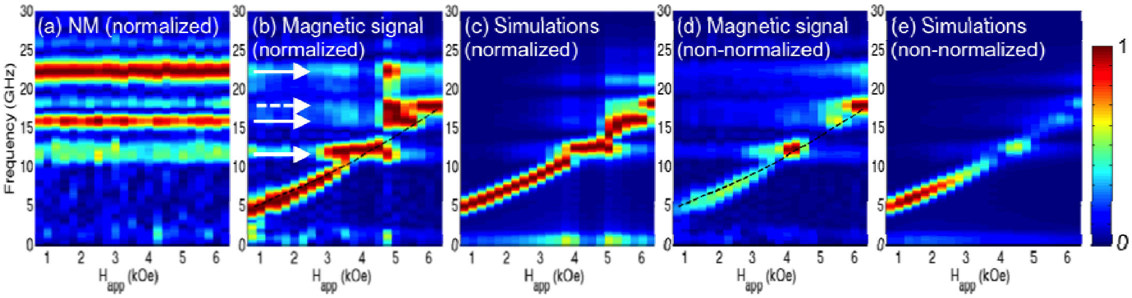

Figure 3 (Color online): Fourier spectra for nickel elliptic disks for p = 212 nm. (a) Measured non-magnetic signal. (b, d) Measured magnetic signal. Dashed line is the simulation result for nickel elliptic disks without magnetoelastic contribution. The solid and dashed arrows in (b) indicate the RW and SSLW frequencies. (c, e) Simulated magnetization dynamics including magnetoelastic coupling. The Fourier amplitudes in (a), (b), and (c) are normalized for better visualization of oscillation modes. The non-normalized Fourier spectra in (d) and (e) illustrate the enhanced Fourier amplitude at the crossover points at 12.2, 15.8, 17.7, and 22.3 GHz.

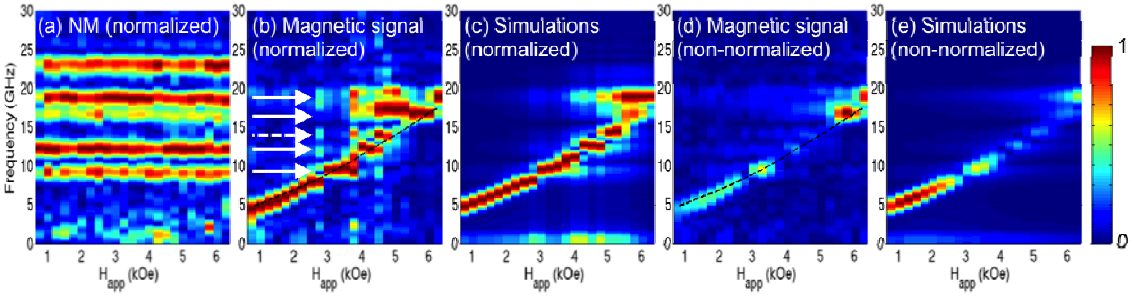

Figure 4 (Color online): Fourier spectra for nickel elliptic disks for p = 282 nm. (a) Measured non-magnetic spectra. (b, d) Measured magnetic spectra. The solid and dashed arrows in (b) indicate the RW and SSLW frequencies. (c, e) Simulated magnetization

dynamics with magnetoelastic coupling. The Fourier amplitudes in (a), (b), and (c) are normalized.